

Limits on non-Gaussianities from WMAP data

Paolo Creminelli^a, Alberto Nicolis^a, Leonardo Senatore^{b,d}
Max Tegmark^d and Matias Zaldarriaga^{a,c}

^a *Jefferson Physical Laboratory,
Harvard University, Cambridge, MA 02138, USA*

^b *Center for Theoretical Physics,
Massachusetts Institute of Technology, Cambridge, MA 02139, USA*

^c *Center for Astrophysics,
Harvard University, Cambridge, MA 02138, USA*

^d *Department of Physics,
Massachusetts Institute of Technology, Cambridge, MA 02139, USA*

Abstract

We develop a method to constrain the level of non-Gaussianity of density perturbations when the 3-point function is of the “equilateral” type. Departures from Gaussianity of this form are produced by single field models such as ghost or DBI inflation and in general by the presence of higher order derivative operators in the effective Lagrangian of the inflaton. We show that the induced shape of the 3-point function can be very well approximated by a factorizable form, making the analysis practical. We also show that, unless one has a full sky map with uniform noise, in order to saturate the Cramer-Rao bound for the error on the amplitude of the 3-point function, the estimator must contain a piece that is linear in the data. We apply our technique to the WMAP data obtaining a constraint on the amplitude $f_{\text{NL}}^{\text{equil.}}$ of “equilateral” non-Gaussianity: $-366 < f_{\text{NL}}^{\text{equil.}} < 238$ at 95% C.L. We also apply our technique to constrain the so-called “local” shape, which is predicted for example by the curvaton and variable decay width models. We show that the inclusion of the linear piece in the estimator improves the constraint over those obtained by the WMAP team, to $-27 < f_{\text{NL}}^{\text{local}} < 121$ at 95% C.L.

1 Introduction

Despite major improvements in the quality of cosmological data over the last few years, there are very few observables that can characterize the early phases of the Universe, when density perturbations

were generated. Deviations from a purely Gaussian statistics of density perturbations would be a very important constraint on models of early cosmology. In single field slow-roll inflation, the level of non-Gaussianity is sharply predicted [1, 2] to be very small, less than 10^{-6} . This is quite far from the present experimental sensitivity. On the other hand, many models have recently been proposed with a much higher level of non-Gaussianity, within reach of present or forthcoming data. For nearly Gaussian fluctuations, the quantity most sensitive to departures from perfect Gaussianity is the 3-point correlation function. In general, each model will give a different correlation between the Newtonian potential modes¹:

$$\langle \Phi(\mathbf{k}_1)\Phi(\mathbf{k}_2)\Phi(\mathbf{k}_3) \rangle = (2\pi)^3 \delta^3(\mathbf{k}_1 + \mathbf{k}_2 + \mathbf{k}_3) F(k_1, k_2, k_3). \quad (1)$$

The function F describes the correlation as a function of the triangle shape in momentum space.

The predictions for the function F in different models divide quite sharply into two qualitatively different classes as a consequence of qualitatively different ways of producing correlations among modes [4]. The first possibility is that the source of density perturbations is not the inflaton but a second light scalar field σ . In this case non-Gaussianities are generated by the non-linear relation between the fluctuation $\delta\sigma$ of this field and the final perturbation Φ we observe. This non-linearity is *local* as it acts when the modes are much outside the horizon; schematically we have $\Phi(\mathbf{x}) = A\delta\sigma(\mathbf{x}) + B(\delta\sigma^2(\mathbf{x}) - \langle \delta\sigma^2 \rangle) + \dots$. Even starting from a purely Gaussian $\delta\sigma$, the quadratic piece introduces a 3-point function for Φ of the form

$$F(k_1, k_2, k_3) = f_{\text{NL}}^{\text{local}} \cdot 2\Delta_{\Phi}^2 \cdot \left(\frac{1}{k_1^3 k_2^3} + \frac{1}{k_1^3 k_3^3} + \frac{1}{k_2^3 k_3^3} \right), \quad (2)$$

where Δ_{Φ} is the power spectrum normalization, $\langle \Phi(\mathbf{k}_1)\Phi(\mathbf{k}_2) \rangle = (2\pi)^3 \delta^3(\mathbf{k}_1 + \mathbf{k}_2) \Delta_{\Phi} \cdot k_1^{-3}$, which for the moment has been taken as exactly scale invariant, and where $f_{\text{NL}}^{\text{local}}$ is proportional to B . Examples of this mechanism are the curvaton scenario [5] and the variable decay width model [6], which naturally give rise to $f_{\text{NL}}^{\text{local}}$ greater than 10 and 5, respectively.

The second class of models are single field models with a non-minimal Lagrangian, where the correlation among modes is created by higher derivative operators [7, 8, 9, 10]. In this case, the correlation is strong among modes with comparable wavelength and it decays when we take one of k 's to zero keeping the other two fixed. Although different models of this class give a different function F , all these functions are qualitatively very similar. We will call this kind of functions *equilateral*: as we will see, the signal is maximal for equilateral configurations in Fourier space, whereas for the local form (2) the most relevant configurations are the *squeezed* triangles with one side much smaller than the others.

The strongest constraint on the level of non-Gaussianity comes from the WMAP experiment. The collaboration analyzed their data searching for non-Gaussianity of the *local* form (2), finding the data to be consistent with purely Gaussian statistics and placing limits on the parameter $f_{\text{NL}}^{\text{local}}$ [11]:

$$-58 < f_{\text{NL}}^{\text{local}} < 134 \quad \text{at 95\% C.L.} \quad (3)$$

¹Even with perfectly Gaussian primordial fluctuations, the observables, *e.g.* the temperature anisotropy, will not be perfectly Gaussian as a consequence of the non-linear relation between primordial perturbations and what we will eventually observe. These effects are usually of order 10^{-5} (see for example [3]) and thus beyond (but not much) present sensitivity. In the following we will disregard these contributions.

The main purpose of this paper is to perform a similar analysis searching for non-Gaussianities of the equilateral form. We can extend the definition of $f_{\text{NL}}^{\text{local}}$ in eq. (2) to a generic function F by setting the overall normalization on equilateral configurations:

$$F(k, k, k) = f_{\text{NL}} \cdot \frac{6\Delta_{\Phi}^2}{k^6}. \quad (4)$$

In this way, two different models with the same f_{NL} will give the same 3-point function for equilateral configurations. For equilateral models in particular, the overall amplitude will be characterized by $f_{\text{NL}}^{\text{equil.}}$. Indirect constraints on $f_{\text{NL}}^{\text{equil.}}$ have been obtained starting from the limit of eq. (3) in [4], resulting in $|f_{\text{NL}}^{\text{equil.}}| \lesssim 800$; we will see that a dedicated analysis is, as expected, much more sensitive. Many of the equilateral models naturally predict sizeable values of the parameter $f_{\text{NL}}^{\text{equil.}}$: ghost inflation and DBI inflation [8, 9] tend to have $f_{\text{NL}}^{\text{equil.}} \sim 100$, tilted ghost inflation $f_{\text{NL}}^{\text{equil.}} \gtrsim 1$ [10], while slow roll inflation with higher derivative coupling typically give $f_{\text{NL}}^{\text{equil.}} \lesssim 1$ [7].

In Section 2 we discuss the main idea of the analysis. We will see that an optimal analysis is numerically very challenging for a generic form of the function F , but simplifies dramatically if the function F is factorizable in a sense that will be defined below. As all the equilateral forms predicted in different models are (qualitatively and quantitatively) very similar, our approach will be to choose a factorizable function that well approximates this class. The analysis is further complicated by the breaking of rotational invariance: a portion of the sky is fully masked by the presence of the galaxy and moreover each point is observed a different number of times. In Section 3 we look for an optimal estimator for f_{NL} . We discover that, unlike the rotationally invariant case, the minimum variance estimator contains not only terms which are cubic in the temperature fluctuations, but also linear pieces. These techniques are used to analyze the WMAP data in Section 4. The result is that the data are compatible with Gaussian statistics. The limit for the equilateral models is

$$-366 < f_{\text{NL}}^{\text{equil.}} < 238 \quad \text{at 95\% C.L.} \quad (5)$$

We also obtain a limit on $f_{\text{NL}}^{\text{local}}$

$$-27 < f_{\text{NL}}^{\text{local}} < 121 \quad \text{at 95\% C.L.} \quad (6)$$

which is a slight improvement with respect to (3) as a consequence of the above-mentioned additional linear piece in the estimator.

2 A factorizable equilateral shape

It is in principle straightforward to generalize the analysis for non-Gaussianities from the local model to another one. We start assuming that the experimental noise on the temperature maps is isotropic and that the entire sky is observed (no Galactic and bright source mask); we will relax these assumptions in the next Section. In this case it can be proved that an optimal estimator \mathcal{E} for f_{NL} exists [12, 13], that is an estimator which saturates the Cramer-Rao inequality and thus gives the strongest possible constraint on the amplitude of the non-Gaussian signal. The estimator \mathcal{E} is a sum of terms cubic in the temperature fluctuations, each term weighted by its signal to noise ratio:

$$\mathcal{E} = \frac{1}{N} \cdot \sum_{l_i m_i} \frac{\langle a_{l_1 m_1} a_{l_2 m_2} a_{l_3 m_3} \rangle}{C_{l_1} C_{l_2} C_{l_3}} a_{l_1 m_1} a_{l_2 m_2} a_{l_3 m_3}. \quad (7)$$

Given the assumptions, the power spectrum C_l (which is the sum of the CMB signal and noise) is diagonal in Fourier space; N is a normalization factor which makes the estimator unbiased. From rotational invariance we can simplify the expression introducing the Wigner $3j$ symbols to

$$\mathcal{E} = \frac{1}{N} \cdot \sum_{l_i m_i} \begin{pmatrix} l_1 & l_2 & l_3 \\ m_1 & m_2 & m_3 \end{pmatrix} \frac{B_{l_1 l_2 l_3}}{C_{l_1} C_{l_2} C_{l_3}} a_{l_1 m_1} a_{l_2 m_2} a_{l_3 m_3} , \quad (8)$$

where $B_{l_1 l_2 l_3}$ is the angle-averaged bispectrum which contains all the information about the model of non-Gaussianity we are considering. If $B_{l_1 l_2 l_3}$ is calculated for $f_{\text{NL}} = 1$, then the normalization factor N is given by

$$N = \sum_{l_1 l_2 l_3} \frac{(B_{l_1 l_2 l_3})^2}{C_{l_1} C_{l_2} C_{l_3}} . \quad (9)$$

We now have to relate the angle-averaged bispectrum to the underlying correlation among 3d modes $F(k_1, k_2, k_3)$. After some manipulations following [14], the estimator takes the form

$$\begin{aligned} \mathcal{E} &= \frac{1}{N} \cdot \sum_{l_i m_i} \int d^2 \hat{n} Y_{l_1 m_1}(\hat{n}) Y_{l_2 m_2}(\hat{n}) Y_{l_3 m_3}(\hat{n}) \int_0^\infty r^2 dr j_{l_1}(k_1 r) j_{l_2}(k_2 r) j_{l_3}(k_3 r) C_{l_1}^{-1} C_{l_2}^{-1} C_{l_3}^{-1} \\ &\int \frac{2k_1^2 dk_1}{\pi} \frac{2k_2^2 dk_2}{\pi} \frac{2k_3^2 dk_3}{\pi} F(k_1, k_2, k_3) \Delta_{l_1}^T(k_1) \Delta_{l_2}^T(k_2) \Delta_{l_3}^T(k_3) a_{l_1 m_1} a_{l_2 m_2} a_{l_3 m_3} , \end{aligned} \quad (10)$$

where $\Delta_l^T(k)$ is the CMB transfer function which relates the a_{lm} to the Newtonian potential $\Phi(k)$:

$$a_{lm} = 4\pi i^l \int \frac{d^3 k}{(2\pi)^3} \Delta_l^T(k) \Phi(k) Y_{lm}^*(\hat{k}) . \quad (11)$$

Equation (10) is valid for any shape of the 3-point function F . Unfortunately this expression is computationally very challenging. The sums over m can be taken inside the integrals and factorized, but we are still left with a triple sum over l of an integral over the sphere. The calculation time grows as $N_{\text{pixels}}^{5/2}$, where the number of pixels N_{pixels} is of order 3×10^6 for WMAP. This approach is therefore numerically too demanding.

As noted in [14], a crucial simplification is possible if the function F is factorizable as a product of functions of k_1 , k_2 and k_3 or can be written as a sum of a small number of terms with this property. In this case the second line of (10) becomes factored as the product of functions of each l separately, so that now also the sum over l can be done before integrating over the sphere. For example if we assume that $F(k_1, k_2, k_3) = f_1(k_1) f_2(k_2) f_3(k_3)$, the estimator simplifies to

$$\mathcal{E} = \frac{1}{N} \cdot \int d^2 \hat{n} \int_0^\infty r^2 dr \prod_{i=1}^3 \sum_{l_i m_i} \int \frac{2k^2 dk}{\pi} j_{l_i}(kr) f_i(k) \Delta_{l_i}^T(k) C_{l_i}^{-1} a_{l_i m_i} Y_{l_i m_i}(\hat{n}) . \quad (12)$$

The calculation is obviously much faster now: it now scales like $N_{\text{pixels}}^{3/2}$ and it is dominated by going back and forth between real and spherical harmonics space. From expression (2) we see that this simplification is possible for the local shape, and it was indeed used for the analysis of the WMAP data in [11, 15].

Unfortunately, none of the ‘‘equilateral models’’ discussed in the Introduction predicts a function F which is factorizable (see some explicit expressions in [4]), so that it is not easy to perform an

optimal analysis for a particular given model. However, all these models give 3-point functions which are quite similar, so that it is a very good approximation to take a factorizable shape function F which is close to the class of functions we are interested in and perform the analysis for this shape. In the limit $k_1 \rightarrow 0$ with k_2 and k_3 fixed, all the equilateral functions diverge as k_1^{-1} [4] (while the local form eq. (2) goes as k_1^{-3}). An example of a function which has this behavior, is symmetric in k_1, k_2 and k_3 , and is a sum of factorizable functions (and is homogeneous of order k^{-6} , see below) is ²

$$F(k_1, k_2, k_3) = f_{\text{NL}}^{\text{equil.}} \cdot 6\Delta_{\Phi}^2 \cdot \left(-\frac{1}{k_1^3 k_2^3} - \frac{1}{k_1^3 k_3^3} - \frac{1}{k_2^3 k_3^3} - \frac{2}{k_1^2 k_2^2 k_3^2} + \frac{1}{k_1 k_2^2 k_3^3} + (5 \text{ perm.}) \right), \quad (14)$$

where the permutations act only on the last term in parentheses. The mild divergence for $k_1 \rightarrow 0$ is achieved through a cancellation among the various terms.

In figure 1, we compare this function with the local shape. The dependence of both functions under a common rescaling of all k 's is fixed to be $\propto k^{-6}$ by scale invariance, so that we can factor out k_1^{-6} for example. Everything will now depend only on the ratios k_2/k_1 and k_3/k_1 , which fix the shape of the triangle in momentum space. For each shape we plot $F(1, k_2/k_1, k_3/k_1)(k_2/k_1)^2(k_3/k_1)^2$; this is the relevant quantity if we are interested in the relative importance of different triangular shapes. The square of this function in fact gives the signal to noise contribution of a particular shape in momentum space [4]. We see that for the function (14), the signal to noise is concentrated on equilateral configurations, while squeezed triangles with one side much smaller than the others are the most relevant for the local shape.

In figure 2 we study the equilateral function predicted both in the presence of higher-derivative terms [7] and in DBI inflation [9]. In the second part of the figure we show the difference between this function and the factorizable one used in our analysis. We see that the relative difference is quite small. The same remains true for other equilateral shapes (see [4] for the analogous plots for other models).

In [4], a ‘‘cosine’’ between different shapes was defined which quantifies how different is the signal given by two distributions. The cosine is calculated from the scalar product of the functions in fig. 1. We can think about this cosine as a sort of correlation coefficient: if the cosine is close to 1 the two shapes are very difficult to distinguish experimentally and an optimal analysis for one of them is very good also for the other. On the other hand, a small cosine means that, once non-Gaussianities are detected, there is a good chance to distinguish the two functions and that an optimal analysis for one shape is not very good for the other. The cosine between our template shape and the functions predicted by equilateral models is very close to one (0.98 with the ghost inflation [8] prediction and

²Eq. (14) can be derived as follows. In order to make the divergence of F mild in the squeezed limit we can use at the numerator a quantity which goes to zero in the same limit. The area of the triangle does the job, going like k_1 for $k_1 \rightarrow 0$. The area can be expressed purely in terms of the sides through Heron’s formula [16], $A = \sqrt{s(s-k_1)(s-k_2)(s-k_3)}$, where $s = \frac{1}{2}(k_1 + k_2 + k_3)$ is the semiperimeter. The first s in the square root is irrelevant for our purposes, since it goes to a constant in the squeezed limit; we will therefore omit it. Also we want a sum of factorizable functions, so we get rid of the square root by considering A^2 . In conclusion, a function with all the features stated above is

$$F(k_1, k_2, k_3) \propto \frac{(s-k_1)(s-k_2)(s-k_3)}{k_1^3 k_2^3 k_3^3}, \quad (13)$$

which, once expanded, reduces exactly to eq. (14).

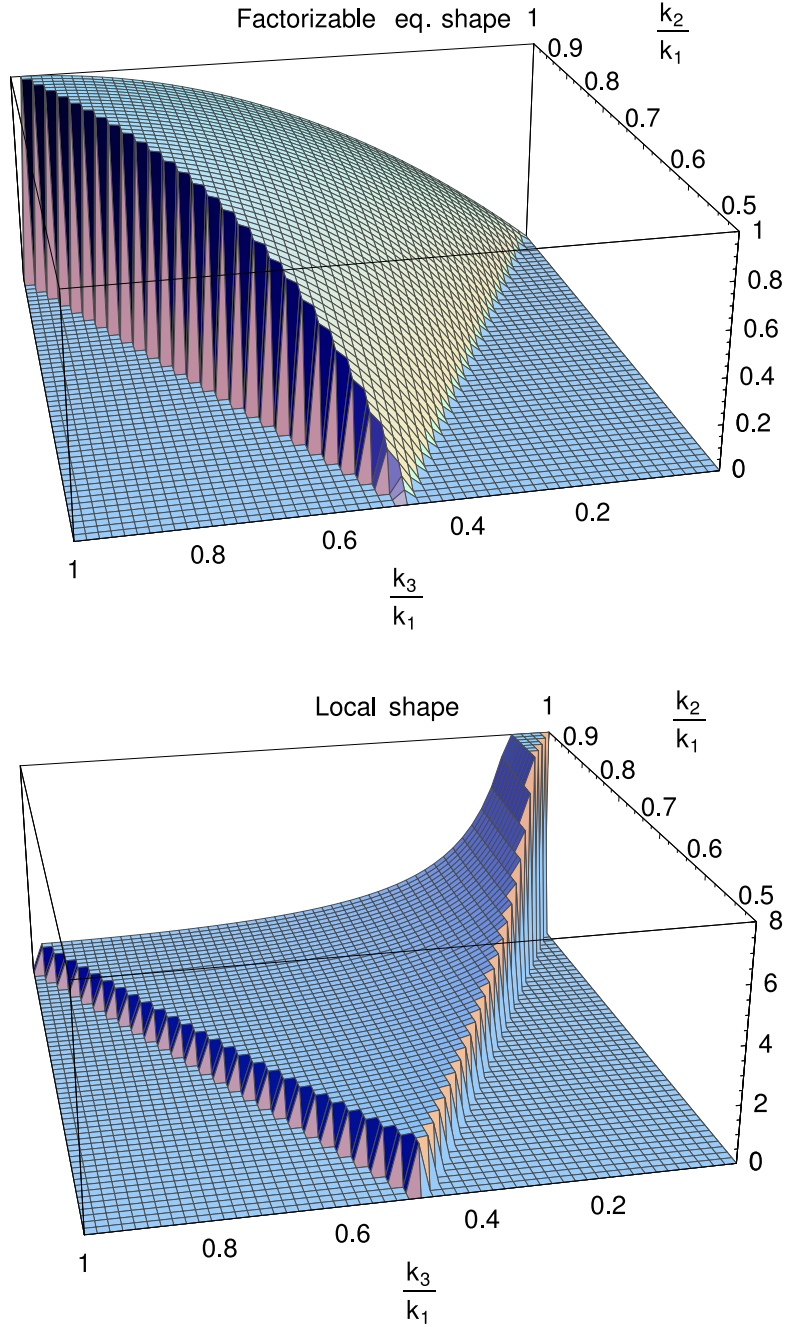


Figure 1: Plot of the function $F(1, k_2/k_1, k_3/k_1)(k_2/k_1)^2(k_3/k_1)^2$ for the equilateral shape used in the analysis (top) and for the local shape (bottom). The functions are both normalized to unity for equilateral configurations $\frac{k_2}{k_1} = \frac{k_3}{k_1} = 1$. Since $F(k_1, k_2, k_3)$ is symmetric in its three arguments, it is sufficient to specify it for $k_1 \geq k_2 \geq k_3$, so $\frac{k_3}{k_1} \leq \frac{k_2}{k_1} \leq 1$ above. Moreover, the triangle inequality says that no side can be longer than the sum of the other two, so we only plot F in the triangular region $1 - \frac{k_2}{k_1} \leq \frac{k_3}{k_1} \leq \frac{k_2}{k_1} \leq 1$ above, setting it to zero elsewhere.

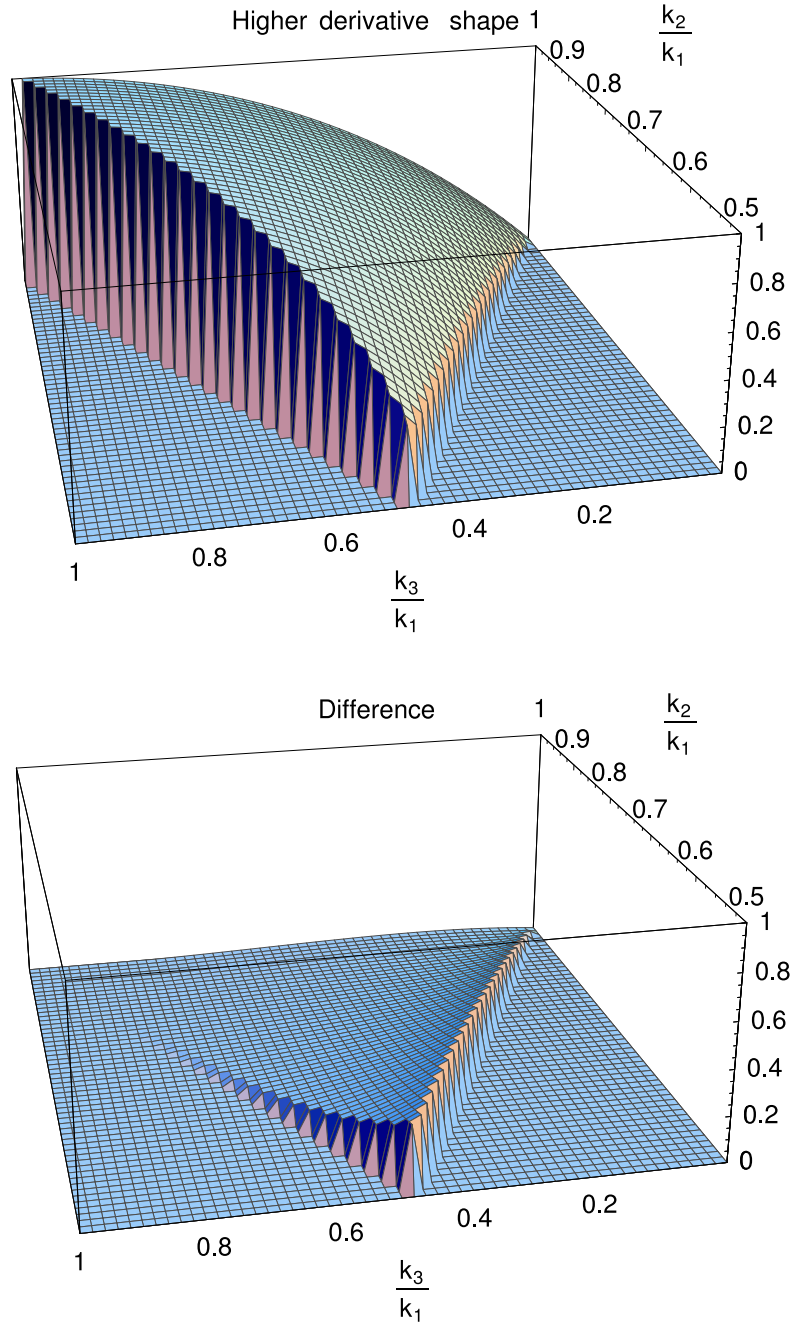


Figure 2: Top. Plot of the function $F(1, k_2/k_1, k_3/k_1)(k_2/k_1)^2(k_3/k_1)^2$ predicted by the higher-derivative [7] and the DBI models [9]. Bottom. Difference between the above plot and the analogous one (top of fig. 1) for the factorizable equilateral shape used in the analysis.

0.99 for higher derivative/DBI models [7, 9]). This means that the error introduced in the analysis by the use of the factorizable shape instead of the correct prediction for a given equilateral model is at the percent level. On the other hand, as evident from figure 1, our template shape is quite different from the local model — the cosine is merely 0.41.

All these numbers are obtained in 3 dimensions assuming that we can directly measure the fluctuations with a 3d experiment like a galaxy survey. The CMB anisotropies are a complicated projection from the 3d modes. This makes it more difficult to distinguish different shapes, although the picture remains qualitatively the same.

Let us proceed with the study of our template shape. To further simplify the estimator in eq. (10), we define the functions

$$\alpha_l(r) \equiv \frac{2}{\pi} \int_0^{+\infty} dk k^2 \Delta_l^T(k) j_l(kr) \quad (15)$$

$$\beta_l(r) \equiv \frac{2}{\pi} \int_0^{+\infty} dk k^{-1} \Delta_l^T(k) j_l(kr) \Delta_\Phi \quad (16)$$

$$\gamma_l(r) \equiv \frac{2}{\pi} \int_0^{+\infty} dk k \Delta_l^T(k) j_l(kr) \Delta_\Phi^{1/3} \quad (17)$$

$$\delta_l(r) \equiv \frac{2}{\pi} \int_0^{+\infty} dk \Delta_l^T(k) j_l(kr) \Delta_\Phi^{2/3} . \quad (18)$$

We use this strange ordering of the functions to keep the notation compatible with [11, 15], where the functions α and β were introduced for the analysis of the local shape. To evaluate \mathcal{E} , we start from the spherical harmonic coefficients of the map a_{lm} and calculate the four maps

$$A(r, \hat{n}) \equiv \sum_{lm} \frac{\alpha_l(r)}{C_l} Y_{lm}(\hat{n}) a_{lm} , \quad B(r, \hat{n}) \equiv \sum_{lm} \frac{\beta_l(r)}{C_l} Y_{lm}(\hat{n}) a_{lm} , \quad (19)$$

$$C(r, \hat{n}) \equiv \sum_{lm} \frac{\gamma_l(r)}{C_l} Y_{lm}(\hat{n}) a_{lm} , \quad D(r, \hat{n}) \equiv \sum_{lm} \frac{\delta_l(r)}{C_l} Y_{lm}(\hat{n}) a_{lm} . \quad (20)$$

Now the estimator \mathcal{E} is given by

$$\mathcal{E} = -\frac{18}{N} \int r^2 dr \int d^2 \hat{n} \left[A(r, \hat{n}) B(r, \hat{n})^2 + \frac{2}{3} D(r, \hat{n})^3 - 2B(r, \hat{n}) C(r, \hat{n}) D(r, \hat{n}) \right] \quad (21)$$

and the normalization N can be calculated from (9) using the explicit form

$$B_{l_1 l_2 l_3} = \sqrt{\frac{(2l_1 + 1)(2l_2 + 1)(2l_3 + 1)}{4\pi}} \begin{pmatrix} l_1 & l_2 & l_3 \\ 0 & 0 & 0 \end{pmatrix} \times \quad (22)$$

$$6 \int_0^\infty r^2 dr [-\alpha_{l_1}(r) \beta_{l_2}(r) \beta_{l_1}(r) + (2 \text{ perm.}) - 2\delta_{l_1}(r) \delta_{l_2}(r) \delta_{l_3}(r) + \beta_{l_1}(r) \gamma_{l_2}(r) \delta_{l_3}(r) + (5 \text{ perm.})] .$$

The functions α , β , γ and δ used in the analysis can be obtained numerically starting from the transfer functions $\Delta_l^T(k)$, which can be computed given a particular cosmological model with publicly available software as CMBFAST [17]. Some plots of these functions are given in fig. 3, where we choose values of r close to $\tau_0 - \tau_R$ (conformal time difference between recombination and the present), as these give the largest contribution to the estimator. The oscillatory behavior induced by the transfer function $\Delta_l^T(k)$ is evident, with a peak at $l \sim 200$. The factors of $l(l+1)$ and $(2l+1)$ in

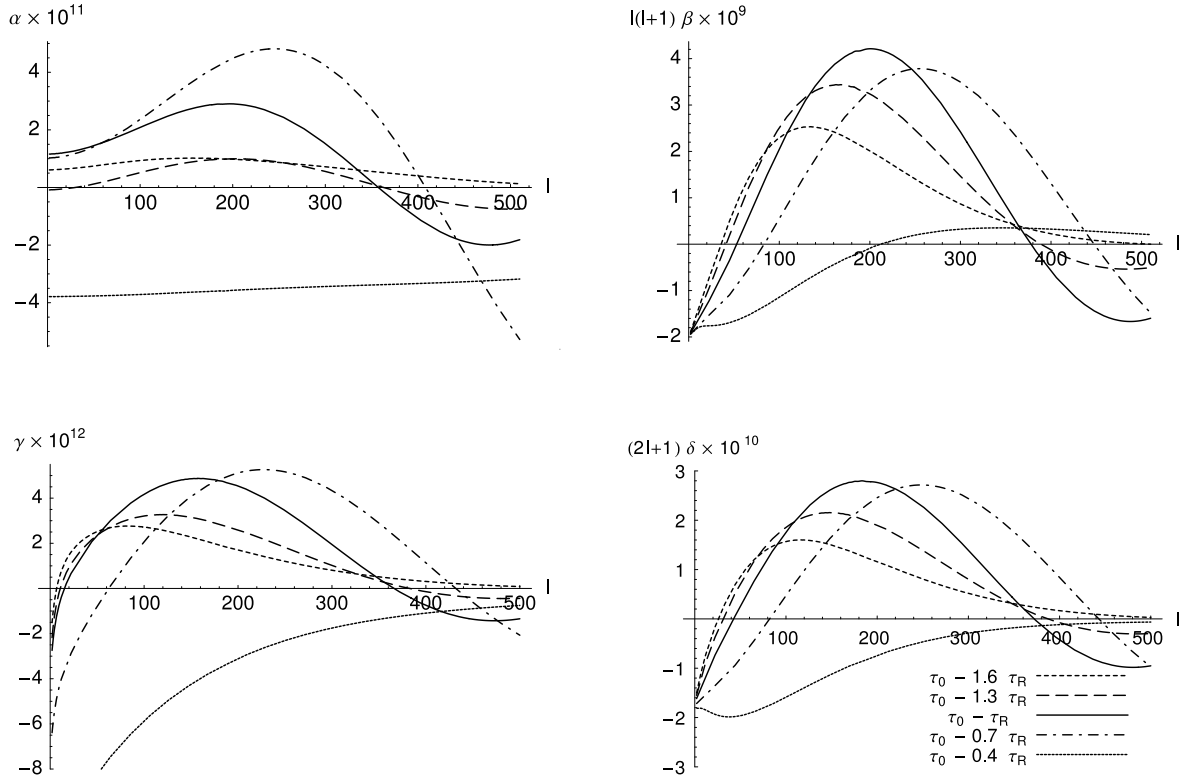


Figure 3: The functions $\alpha_l(r)$ (in units of Mpc^{-3}), $\beta_l(r)$ (dimensionless), $\gamma_l(r)$ (in units of Mpc^{-2}), and $\delta_l(r)$ (in units of Mpc^{-1}) are shown for various radii r as functions of the multipole number l . The cosmological parameters are the same ones used in the analysis: $\Omega_b h^2 = 0.024$, $\Omega_m h^2 = 0.14$, $h = 0.72$, $\tau = 0.17$. With these parameters, the present conformal time τ_0 is 13.24 Gpc and the recombination time τ_R is 0.27 Gpc.

the β and δ functions, respectively, can be understood from the behavior at low l 's, in the Sachs-Wolfe regime. Here the transfer function can be approximated by $\Delta_l^T(k) = -j_l(k(\tau_0 - \tau_R))/3$, and we then see that $\beta_l(\tau_0 - \tau_R) \propto \int_0^\infty dk k^{-1} j_l^2(k(\tau_0 - \tau_R)) \propto 1/(l(l+1))$ and $\delta_l(\tau_0 - \tau_R) \propto \int_0^\infty dk j_l^2(k(\tau_0 - \tau_R)) \propto 1/(2l+1)$. From these expressions we also see that the function β (the only one which is dimensionless) is very similar to the C_l^{cmb} 's as, in the Sachs-Wolfe regime, $C_l^{\text{cmb}} \simeq \frac{2}{9\pi} \int_0^\infty dk k^{-1} \Delta_\Phi j_l^2(k(\tau_0 - \tau_R))$.

3 Optimal estimator for f_{NL}

There are two quite general experimental complications that make the estimator \mathcal{E} defined in the last Section non-optimal. First, foreground emission from the Galactic plane and from isolated bright sources contaminates a substantial fraction of sky, which must be masked out before the analysis [18]. This projection which can be accomplished by giving very large noise to regions that are affected by foregrounds, besides reducing the available amount of data, has the important effect of breaking rotational invariance, so that the signal covariance matrix $C_{l_1 m_1, l_2 m_2}^{\text{cmb}}$ of the masked sky becomes non-diagonal in multipole space. Second, the noise level is not the same in different regions of the

sky, because the experiment looks at different regions for different amounts of time. This implies that also the noise covariance matrix $C_{l_1 m_1, l_2 m_2}^{\text{noise}}$ is non-diagonal in multipole space. The importance of the anisotropy of the noise was pointed out in [11], as it caused an increase of the variance of the estimator \mathcal{E} at high l 's.

For these reasons, it is worth trying to generalize the estimator \mathcal{E} . We consider estimators for f_{NL} (for a given shape of non-Gaussianities) which contain both trilinear and linear terms in the a_{lm} 's. In the rotationally invariant case, a linear piece in the estimator can only be proportional to the monopole, which is unobservable. However, in the absence of rotational invariance, linear terms can be relevant. In this class, it is straightforward to prove that the unbiased estimator with the smallest variance is given by

$$\begin{aligned} \mathcal{E}_{\text{lin}}(a) = & \frac{1}{N} \sum_{l_i m_i} \left(\langle a_{l_1 m_1} a_{l_2 m_2} a_{l_3 m_3} \rangle_1 C_{l_1 m_1, l_4 m_4}^{-1} C_{l_2 m_2, l_5 m_5}^{-1} C_{l_3 m_3, l_6 m_6}^{-1} a_{l_4 m_4} a_{l_5 m_5} a_{l_6 m_6} \right. \\ & \left. - 3 \langle a_{l_1 m_1} a_{l_2 m_2} a_{l_3 m_3} \rangle_1 C_{l_1 m_1, l_2 m_2}^{-1} C_{l_3 m_3, l_4 m_4}^{-1} a_{l_4 m_4} \right), \end{aligned} \quad (23)$$

where N is a normalization factor:

$$N = \sum_{l_i m_i} \langle a_{l_1 m_1} a_{l_2 m_2} a_{l_3 m_3} \rangle_1 C_{l_1 m_1, l_4 m_4}^{-1} C_{l_2 m_2, l_5 m_5}^{-1} C_{l_3 m_3, l_6 m_6}^{-1} \langle a_{l_4 m_4} a_{l_5 m_5} a_{l_6 m_6} \rangle_1. \quad (24)$$

The averages $\langle \dots \rangle_1$ are taken with $f_{\text{NL}} = 1$. As we stressed, the covariance matrix $C = C^{\text{cmb}} + C^{\text{noise}}$ contains the effects of the mask projection and the anisotropic noise and it is thus non-diagonal in multipole space.

It turns out that the estimator \mathcal{E}_{lin} saturates the Cramer-Rao bound, *i.e.* it is not only optimal in its class, but it is also the minimum variance unbiased estimator among all the possible ones. To prove this, we expand the probability distribution in the limit of weak non-Gaussianity (which is surely a good approximation for the CMB) using the Edgeworth expansion [19, 20, 21].

$$P(a|f_{\text{NL}}) = \left(1 - f_{\text{NL}} \sum_{l_i m_i} \langle a_{l_1 m_1} a_{l_2 m_2} a_{l_3 m_3} \rangle_1 \frac{\partial}{\partial a_{l_1 m_1}} \frac{\partial}{\partial a_{l_2 m_2}} \frac{\partial}{\partial a_{l_3 m_3}} \right) \frac{e^{-\frac{1}{2} \sum a_{l_4 m_4}^* C_{l_4 m_4, l_5 m_5}^{-1} a_{l_5 m_5}}}{\sqrt{(2\pi)^N \det(C)}}. \quad (25)$$

Now, following the same arguments of [13] which considered the same problem in the rotationally invariant case, the estimator is optimal (in the sense that its variance saturates the Cramer-Rao bound), if and only if the following condition is satisfied:

$$\frac{d \log P(a|f_{\text{NL}})}{d f_{\text{NL}}} = F(f_{\text{NL}}) (\mathcal{E}_{\text{lin}}(a) - f_{\text{NL}}), \quad (26)$$

where $F(f_{\text{NL}})$ is a generic function³ of the parameter f_{NL} . From the probability distribution (25) it is easy to check that the estimator \mathcal{E}_{lin} is proportional to $d \log P(a|f_{\text{NL}})/d f_{\text{NL}}$ in the limit of small f_{NL} . We conclude that \mathcal{E}_{lin} is an optimal estimator for a nearly Gaussian distribution.

We now want to make some approximations to the optimal estimator \mathcal{E}_{lin} to make it numerically easier to evaluate. The full inversion of the covariance matrix is computationally rather cumbersome (although doable as the matrix is with good approximation block diagonal [22]). We therefore

³When eq. (26) is satisfied, the function F turns out to be the Fisher information for the parameter f_{NL} , $F(f_{\text{NL}}) = \langle (d \log P(a|f_{\text{NL}})/d f_{\text{NL}})^2 \rangle$.

approximate $C^{-1}a$ in the trilinear term of eq. (23) by masking out the sky before computing the a_{lm} 's and taking C as diagonal:

$$\text{trilinear} \rightarrow \frac{1}{N} \sum_{l_i m_i} \frac{\langle a_{l_1 m_1} a_{l_2 m_2} a_{l_3 m_3} \rangle_1}{C_{l_1} C_{l_2} C_{l_3}} a_{l_1 m_1} a_{l_2 m_2} a_{l_3 m_3} , \quad (27)$$

where $\langle a_{l_1 m_1} a_{l_2 m_2} a_{l_3 m_3} \rangle_1$ is still given by the full sky expressions of the last Section. Once we have made this approximation for the trilinear term it is easy to prove that the choice for the linear term which minimizes the variance is

$$\text{linear} \rightarrow -\frac{3}{N} \sum_{l_i m_i} \frac{\langle a_{l_1 m_1} a_{l_2 m_2} a_{l_3 m_3} \rangle_1}{C_{l_1} C_{l_2} C_{l_3}} C_{l_1 m_1, l_2 m_2} a_{l_3 m_3} . \quad (28)$$

Note that we must not approximate the covariance matrix C in the numerator as diagonal. This would leave only a term proportional to the monopole a_{00} (which is unobservable), as in the rotationally invariant case.

The normalization factor N is given by

$$N = f_{\text{sky}} \sum_{l_1 l_2 l_3} \frac{(B_{l_1 l_2 l_3})^2}{C_{l_1} C_{l_2} C_{l_3}} , \quad (29)$$

where f_{sky} is the fraction of the sky actually observed. As shown in [23], this correctly takes into account the reduction of data introduced by the mask for multipoles much higher than the inverse angular scale of the mask. The accuracy of this approximation has been checked on non-Gaussian simulations for the local shape in [11].

Let us try to understand qualitatively the effect of the linear correction. Take a large region of the sky that has been observed many times so that its noise level is low. This region will therefore have a small-scale power lower than average. Now, in a given realization depending on how the large scale modes look like, this long-wavelength modulation of the small-scale power spectrum may be “misinterpreted” by the trilinear estimator as a non-Gaussian signal. Indeed, for the local shape, most of the signal comes precisely from the correlation between long wavelength modes and the small scale power [4]. On the other hand, for equilateral shapes, as we noted, the signal is quite low on squeezed configurations so that we expect this effect to be small. The linear term measures the correlation between a given map and the anisotropies in the power spectrum, thus correcting for this spurious signal. Clearly the spurious correlation is zero on average, but the effect increases the variance of the estimator.

We will apply the linear correction of the estimator only for the local shape, since, as we will verify later, it gives a very small effect for equilateral shapes. Following the same steps as in the last Section to factorize the trilinear term in the estimator, we get an explicit expression for the linear piece in the local case:

$$-\frac{3}{N} \int r^2 dr \int d^2 \hat{n} \sum_{l_3 m_3} \left(2S_{AB}(\hat{n}, r) \frac{\beta_{l_3}(r)}{C_{l_3}} Y_{l_3, m_3}(\hat{n}) + S_{BB}(\hat{n}, r) \frac{\alpha_{l_3}(r)}{C_{l_3}} Y_{l_3, m_3}(\hat{n}) \right) a_{l_3 m_3} , \quad (30)$$

where the two maps $S_{AB}(\hat{n}, r)$ and $S_{BB}(\hat{n}, r)$ are defined as

$$S_{AB}(\hat{n}, r) = \sum_{l_i m_i} \frac{\alpha_{l_1}(r)}{C_{l_1}} Y_{l_1, m_1}(\hat{n}) \frac{\beta_{l_2}(r)}{C_{l_2}} Y_{l_2, m_2}(\hat{n}) \langle a_{l_1 m_1} a_{l_2 m_2} \rangle , \quad (31)$$

$$S_{BB}(\hat{n}, r) = \sum_{l_i m_i} \frac{\beta_{l_1}(r)}{C_{l_1}} Y_{l_1, m_1}(\hat{n}) \frac{\beta_{l_2}(r)}{C_{l_2}} Y_{l_2, m_2}(\hat{n}) \langle a_{l_1 m_1} a_{l_2 m_2} \rangle. \quad (32)$$

As discussed above, it is only the anisotropic part of the matrix $\langle a_{l_1 m_1} a_{l_2 m_2} \rangle$ that gives a contribution to the linear part of the estimator. This matrix can be decomposed as

$$\langle a_{l_1 m_1} a_{l_2 m_2} \rangle = \langle a_{l_1 m_1}^{\text{cmb}} a_{l_2 m_2}^{\text{cmb}} \rangle + \langle a_{l_1 m_1}^{\text{noise}} a_{l_2 m_2}^{\text{noise}} \rangle, \quad (33)$$

where a_{lm}^{cmb} are the a_{lm} 's of a map generated with CMB signal only and then performing the mask projection, and a_{lm}^{noise} are the ones associated with a map generated with noise only and then performing the mask projection. Both of these two matrices have an anisotropic component. For the map $\langle a_{l_1 m_1}^{\text{cmb}} a_{l_2 m_2}^{\text{cmb}} \rangle$, this arises only because of the sky cut, while for the map $\langle a_{l_1 m_1}^{\text{noise}} a_{l_2 m_2}^{\text{noise}} \rangle$, it is generated both by the sky cut and by the anisotropy of the noise power. We already discussed about the effect of the anisotropy of the noise in the previous paragraph; this effect turns out to be the most relevant. The sky cut gives a much smaller effect because, as we will explain more in detail in the next Section, it is mainly associated with the average value of the temperature outside of the sky cut, and this average value is subtracted out before the analysis.

4 Analysis of WMAP 1-year data

We keep our methodology quite similar to the one used by the WMAP collaboration for their analysis of the local shape [11] in order to have a useful consistency check. We compare WMAP data with Gaussian Monte-Carlo realizations, which are used to estimate the variance of the estimator. We generate with HEALPix⁴ a random CMB realization, with fixed cosmological parameters, at resolution $n_{\text{side}}=256$ (786,432 pixels). The parameters are fixed to the WMAP best fit for a Λ CDM cosmology with power-law spectrum [24]: $\Omega_b h^2 = 0.024$, $\Omega_m h^2 = 0.14$, $h = 0.72$, $\tau = 0.17$, $n_s = 0.99$. With these parameters, the present conformal time τ_0 is 13.24 Gpc and the recombination time is $\tau_R = 0.27$ Gpc. A given realization is smoothed with the WMAP window functions for the Q1, Q2, V1, V2, W1, W2, W3 and W4 bands [25]. To each of these 8 maps we add an independent noise realization: for every pixel the noise is a Gaussian random variable with variance $\sigma_0^2/N_{\text{obs}}$, where N_{obs} is the number of observations of the pixel and σ_0 is a band dependent constant [26]. The maps are then combined to give a single map: we make a pixel by pixel average of the 8 maps weighted by the noise $\sigma_0^2/N_{\text{obs}}$. We use this procedure because it is identical to that used in [11], thereby allowing direct comparisons between our results and those of the WMAP team. In future work, it can in principle be improved in two ways. First of all, for the window function to be strictly rather than approximately uniform across the sky, the weights of the eight input maps should be constant rather than variable from pixel to pixel. This is a very small effect in practice, since the eight N_{obs} -maps are very similar, making the weights close to constant. Second, the sensitivity on small scales can be improved by using l -dependent weights [27]: for instance, at very high l , most of the weight should be given to the W bands, since they have the narrowest beam. This would also have a small effect for our particular application, since our estimator uses only the first few hundred multipoles. We explicitly checked that this would not reduce the variance of our estimator appreciably.

⁴See HEALPix website: <http://www.eso.org/science/healpix/>

We apply the $Kp0$ mask to the final map, to cut out the Galactic plane and the known point sources [18]: this mask leaves the 76.8% of the pixels, $f_{\text{sky}} = 0.768$. The average temperature outside the mask is then subtracted.

On the resulting map we calculate the estimators defined in the preceding Sections. For the local shape we performed the analysis both with and without the linear piece discussed in Section 3. The quadratic maps of equations (31) and (32) used for the linear correction are calculated by averaging many ($\simeq 600$) Monte-Carlo maps obtained with the same procedure above. We use HEALPix to generate and analyze maps at resolution level $n_{\text{side}}=256$ (786,432 pixels). The integration over r is performed from $\tau_0 - 0.025 \tau_R$ up to $\tau_0 - 2.5 \tau_R$ with ~ 200 equidistant points, and then with another logarithmically spaced ~ 60 points up to the present epoch. Such a high resolution both in r spacing and in n_{side} is necessary in order to reproduce the cancellation on squeezed triangles which occurs among the various terms in the equilateral shape (14). The computation of each f_{NL} on a 2.0 GHz Opteron processor with 2 GB of RAM takes about 60 minutes for the local shape, and 100 minutes for the equilateral shape.

We then apply exactly the same procedure to WMAP data. These maps are analyzed after template foreground corrections are applied, in order to reduce foreground signal leaking outside the mask, as described in [18].

A useful analytic bound on the variance of the estimators for $f_{\text{NL}}^{\text{local}}$ and $f_{\text{NL}}^{\text{equil.}}$ is obtained from the variance of the full sky estimator (with homogeneous noise) (8) with an f_{sky} -correction which takes into account the reduction in available information from not observing the whole sky. Taking into account the normalization factor, one readily obtains

$$\sigma_{\text{an}}^{-2} = f_{\text{sky}} \sum_{l_1 < l_2 < l_3} \frac{B_{l_1 l_2 l_3}^2}{C_{l_1} C_{l_2} C_{l_3}}, \quad (34)$$

where $B_{l_1 l_2 l_3}$ must be evaluated for $f_{\text{NL}}^{\text{local}}$ or $f_{\text{NL}}^{\text{equil.}}$ equal to 1. As we discussed, our approach is not strictly optimal as we are not inverting the full covariance matrix, so we expect σ_{an} to be smaller than the actual standard deviation that we measure from our Monte-Carlos.

In figure 4, we show the standard deviation of estimators for the local shape parameter $f_{\text{NL}}^{\text{local}}$ as a function of the maximum multipole analyzed. We compare the results of our Monte-Carlo simulations (with and without the linear correction) with the analytic bound discussed above. The results without linear correction are compatible with the analysis in [11]. We see that the addition of the linear piece reduces the variance divergence at high l 's. The residual divergence is probably associated with the fact that we did not invert the full covariance matrix. The estimator with the smallest variance is the one with linear correction at $l_{\text{max}} = 335$, with a standard deviation of 37. The analytic approximation has an asymptotic value of 30 which should be considered the best possible limit with the present data. Our estimator thus extracts about $(37/30)^{-2} \approx 66\%$ of the $f_{\text{NL}}^{\text{local}}$ -information (inverse variance) from the WMAP data. The analysis of the data with $l_{\text{max}} = 335$ gives 47, so there is no evidence of deviation from pure Gaussianity and we can set a 2σ limit of

$$-27 < f_{\text{NL}}^{\text{local}} < 121 \quad \text{at } 95\% \text{ C.L.} \quad (35)$$

In fig. 5, we show a map $S_{AB}(\hat{n}, r)$ for a radius around recombination calculated with noise only and for $l_{\text{max}} = 370$, as an illustrative example of the role of the linear piece. As we will clarify below, it is in fact the anisotropy of the noise that causes most of the contribution to the linear piece. The

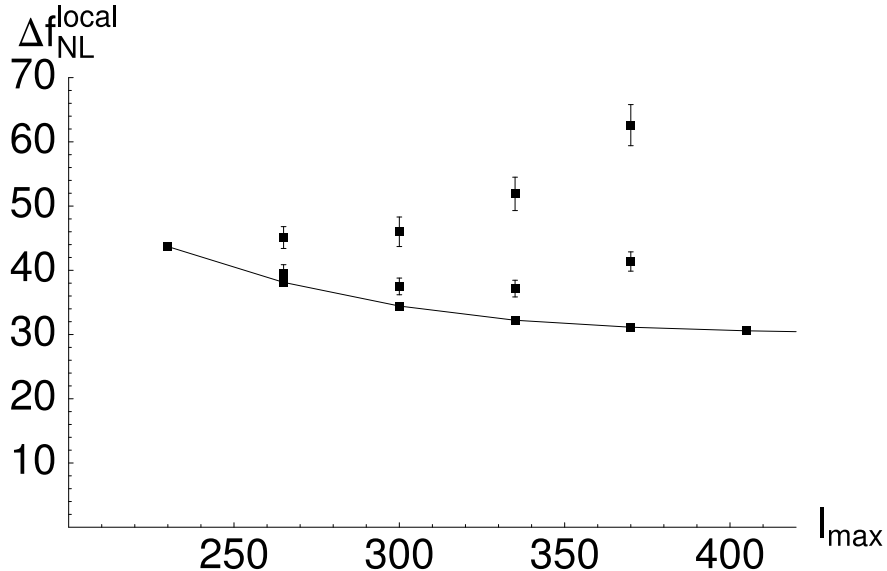


Figure 4: Standard deviation for estimators of $f_{\text{NL}}^{\text{local}}$ as a function of the maximum l used in the analysis. Lower curve: lower bound deduced from the full sky variance. Lower data points: standard deviations for the trilinear + linear estimator. Upper data points: the same for the estimator without linear term, for which the divergence at high l 's caused by noise anisotropy had already been noticed in [11].

companion map $S_{BB}(\hat{n}, r)$ is qualitatively very similar to the map S_{AB} . It is the anisotropy of the noise that gives rise to a non-trivial (*i.e.* non-uniform) S_{AB} map, as is clear from the comparison in the same figure with a plot of the number of observations per pixel. This can help us in understanding the contribution of the linear piece associated with the anisotropy of the noise to the estimator. Let us consider a particular Gaussian Monte Carlo realization with a long wavelength mode crossing one of the regions with a high number of observations. The trilinear piece of the estimator will then detect a spurious non-Gaussian signal associated with the correlation between this long wavelength mode and the small short scale power of the noise ⁽⁵⁾. The maps S_{AB} and S_{BB} , because of their particular shape, will have a non-zero dot product with precisely the same long wavelength mode of the Monte Carlo map, and with an amplitude proportional to the anisotropy of the two point function of the noise, thus effectively subtracting the spurious signal detected by the trilinear piece and reducing the variance of the estimator.

As the mask breaks rotational invariance, the CMB signal also gives non-uniform S -maps. However, the breaking of rotational invariance can be neglected far from the galaxy mask, so we expect that the contribution to the S -maps from the CMB is to first approximation constant outside the mask (and zero inside). In this approximation, the linear contribution of the estimator would be sensitive only to the average value outside the mask. However, given that we are constraining the

⁵The effect of this spurious signal obviously averages to zero among many Monte Carlo realizations but it increases the variance of the estimator.

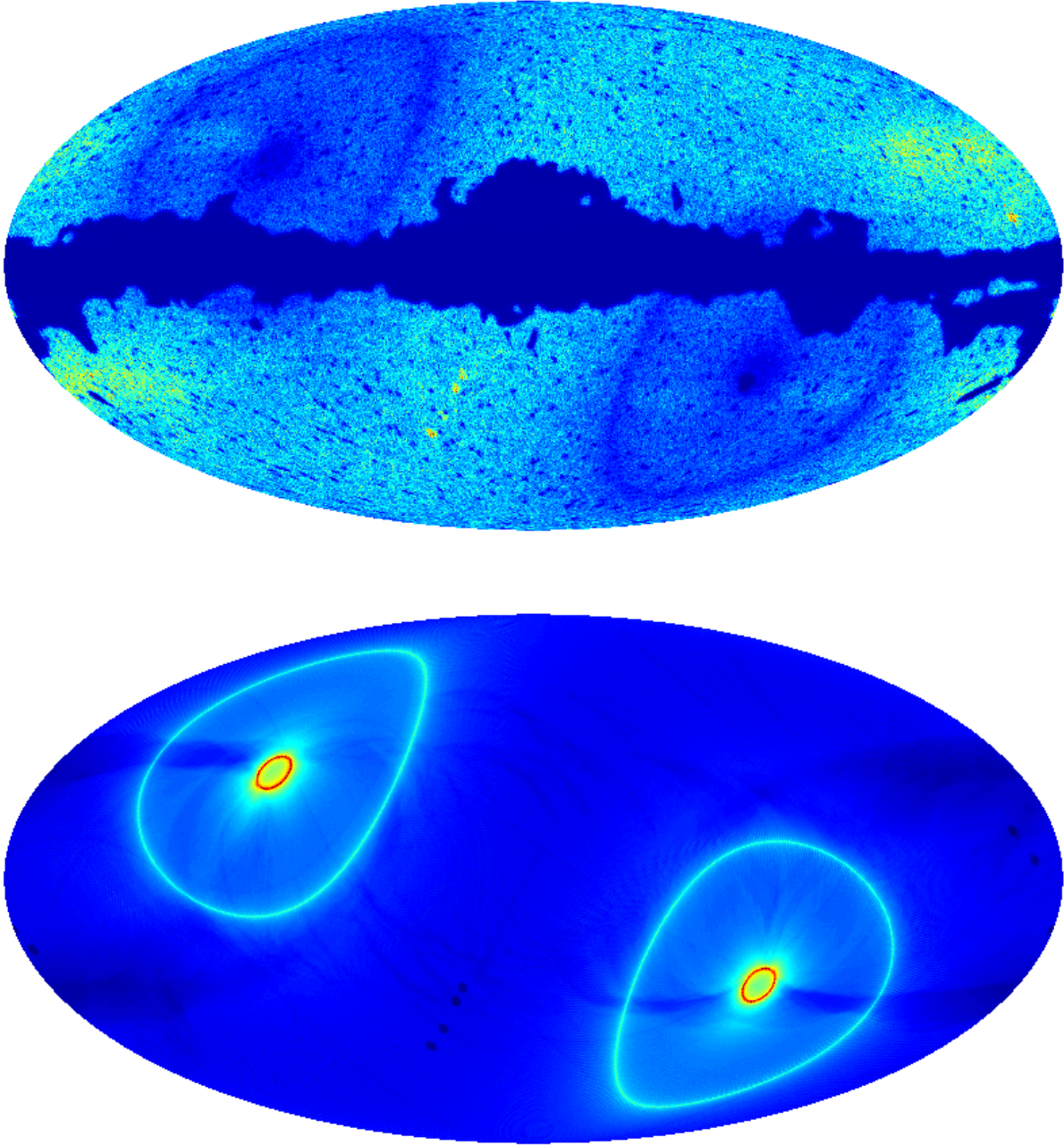


Figure 5: Top: $S_{AB}(\hat{n}, r)$ map for r around recombination calculated with noise only. Bottom: number of observations as a function of the position in the sky for the Q1 band (the plot is quite similar for the other bands). A lighter color indicates points which are observed many times.

statistical properties of temperature fluctuations, the average temperature in the region outside the mask has to be subtracted before performing the analysis; therefore we expect the linear correction associated with the CMB signal to be rather small. These expectations are in fact verified by our simulations. We checked that the maps S coming from the CMB signal are to first approximation constant outside the mask, with additional features coming from the patches used to mask out bright

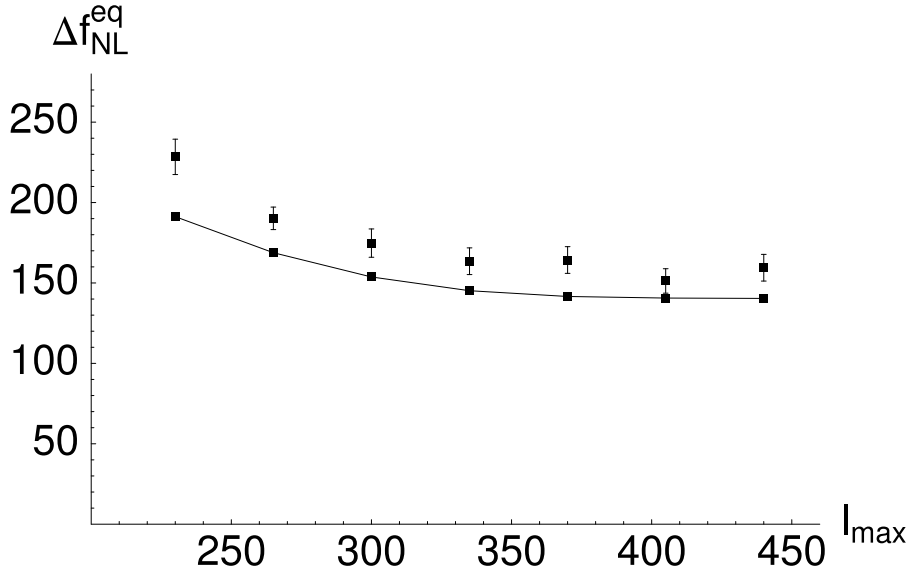


Figure 6: Standard deviations for estimators of $f_{\text{NL}}^{\text{equil.}}$ as a function of the maximum l used in the analysis. Lower curve: lower bound deduced from the full sky variance. Data points: standard deviations for the estimator without linear term.

sources outside the Galactic plane. We then verified that if the average value of the temperature is not subtracted, the linear term coming from the CMB signal gives a very important reduction of the estimator variance, while its effect is almost negligible when the mean temperature is subtracted, as we do in the analysis.

In figure 6, we study the standard deviation of the estimators for $f_{\text{NL}}^{\text{equil.}}$. The estimator without linear corrections is quite close to the information-theoretical limit, so we did not add the linear corrections (which would require many averages analogous to the maps S_{AB} and S_{BB}). The reason why we have such a good behavior is that, as mentioned, here most of the signal comes from equilateral configurations. Thus the estimator is not very sensitive to the correlation between the short scale power and the (long wavelength) number of observations. Moreover the inversion of the covariance matrix is important only for the low multipoles, which give only a small fraction of the signal for $f_{\text{NL}}^{\text{equil.}}$. We find that the estimator with smallest standard deviation is at $l_{\max} = 405$, with a standard deviation of 151. The analysis of the data with the same l_{\max} gives -64 . We deduce a 2σ limit

$$-366 < f_{\text{NL}}^{\text{equil.}} < 238 \quad \text{at } 95\% \text{ C.L.} \quad (36)$$

The given limit is approximately 2 times stronger than the limit obtained in [4], indirectly obtained starting from the limit on $f_{\text{NL}}^{\text{local}}$. The limit appears weaker than for the local case because, for the same f_{NL} , the local distribution has larger signal to noise ratio than an equilateral one, as evident from fig. 1. This is not a physical difference but merely a consequence of our defining f_{NL} at the equilateral configuration.

To check that the two limits correspond approximately to the same “level of non-Gaussianity”

we can define a quantity which is sensitive to the 3-point function integrated over all possible shapes of the triangle in momentum space. In this way it will be independent of which point we choose for normalization. We define this quantity, which we will call NG, directly in 3d as an integral of the square of the functions in fig. 1

$$\text{NG} \equiv \left(\int_{\Delta} \frac{x_2 dx_2 x_3 dx_3}{(2\pi)^2} \frac{F(1, x_2, x_3)^2}{\Delta_{\Phi}^3 x_2^{-3} x_3^{-3}} \right)^{1/2}. \quad (37)$$

The integration is restricted to the same triangular region as in fig.s 1 and 2: $1 - x_2 \leq x_3 \leq x_2 \leq 1$. The measure of integration comes from the change of variables from the 3d wavevectors to the ratios $x_2 = k_2/k_1$ and $x_3 = k_3/k_1$. NG is parametrically of order $\Delta_{\Phi}^{1/2} \cdot f_{\text{NL}}$ (where $\Delta_{\Phi} \simeq 1.9 \cdot 10^{-8}$ [24, 28]), which is the correct order of magnitude of the non-Gaussianity, analogous to the skewness for a single random variable. To better understand the meaning of the defined quantity, note that if we integrate inside the parentheses in eq. (37) over the remaining wavevector we get the total signal to noise ratio (or better the non-Gaussian to Gaussian ratio). This further integration would approximately multiply NG by the square root of the number of data. This means that to detect a given value of NG we need a number of data of order NG^{-2} , in order to have a signal to noise ratio of order 1. This is clearly a good way to quantify the deviation of the statistics from pure Gaussianity. The 2σ windows for f_{NL} can be converted to constraints on NG (we define NG to have the same sign of f_{NL})⁶

$$-0.006 < \text{NG}^{\text{local}} < 0.025 \quad \text{at } 95\% \text{ C.L.} \quad (38)$$

$$-0.016 < \text{NG}^{\text{equil.}} < 0.010 \quad \text{at } 95\% \text{ C.L.} \quad (39)$$

Contrary to what one might think from a naive look at the limits on f_{NL} , the maximum tolerated amount of non-Gaussian signal in a map is thus very similar for both shapes.

So far in this paper, we have neglected any possible dependence on the cosmological parameters. A proper analysis would marginalize over our uncertainties in parameters and this would increase the allowed range of f_{NL} . In order to estimate what the effect of these uncertainties is, let us imagine that the real cosmological parameters are not exactly equal to the best fit ones. The cosmological parameters are determined mainly from the 2-point function of the CMB, C_l^{cmb} , therefore the largest error bars are associated to those combinations of parameters which leave C_l^{cmb} unchanged. In the limit in which the C_l^{cmb} 's remain the same, also the variance of our estimator (which is computed with the best fit cosmological parameters for a Λ CDM cosmology with power-law spectrum [24]) remains the same: in the weak non-Gaussian limit the variance just depends on the 2-point function. However, the combination of parameters which leave unchanged the C_l^{cmb} 's does not necessarily leave unchanged the bispectrum, therefore uncertainties in the determination of the cosmological parameters will have an influence on the expectation value of the estimator. The expectation value of the estimator would be:

$$\langle \mathcal{E} \rangle = \frac{1}{N} \sum_{l_1 < l_2 < l_3} \frac{B_{l_1 l_2 l_3} \tilde{B}_{l_1 l_2 l_3}}{C_{l_1} C_{l_2} C_{l_3}}, \quad (40)$$

⁶Note that for the local model the integration in eq. (37) diverges like the log of the ratio of the minimum to the maximum scales in the integral. For the quoted numbers we chose a ratio of 1000.

where N , $B_{l_1 l_2 l_3}$ and C_l are the same as in our analysis, computed with the best fit cosmological parameters, while $\tilde{B}_{l_1 l_2 l_3}$ is the true bispectrum. Thus when varying parameters, the normalization N needs to be changed to make the estimator unbiased.

The most relevant uncertainty is the reionization optical depth τ , which is correlated with the uncertainty in the amplitude of the power spectrum Δ_Φ . With the purpose of having a rough estimate, we can approximate the effect of reionization by a multiplicative factor $e^{-\tau}$ in front of the transfer function $\Delta_l^T(k)$ for l corresponding to scales smaller than the horizon at reionization. In order to keep the C_l^{cmb} 's unchanged, at least at high l 's, we then multiply Δ_Φ by $e^{2\tau}$. The bispectrum is proportional to $\Delta_\Phi^2 \Delta_l^T(k)^3$ and thus changes even if the C_l 's do not. For the equilateral shape most of the signal comes from equilateral configurations with all the 3 modes inside the horizon at reionization; in this case $\langle \mathcal{E} \rangle$ scales roughly as e^τ . For the local shape the signal comes from squeezed configurations with one mode of much smaller wavelength than the others. Taking only 2 modes inside the horizon at reionization we get $\langle \mathcal{E} \rangle \propto e^{2\tau}$.

If we consider the 1σ error, $\tau = 0.166_{-0.071}^{+0.076}$ [24], we find that the uncertainty in the reionization depth should correspond to an error on f_{NL} of order 8% for the equilateral shape, and 15% for the local shape. These numbers translate directly into uncertainties in the allowed ranges we quote. In the future, if the error induced by the uncertainty in the cosmological parameters will become comparable to the variance of the estimator, a more detailed analysis will be required; however, at the moment an analysis with fixed cosmological parameters is certainly good enough.

5 Conclusions

We have developed a method to constrain the level of non-Gaussianity when the induced 3-point function is of the ‘‘equilateral’’ type. We showed that the induced shape of the 3-point function can be very well approximated by a factorizable form making the analysis practical. Applying our technique to the WMAP first year data we obtained

$$-366 < f_{\text{NL}}^{\text{equil.}} < 238 \quad \text{at 95\% C.L.} \quad (41)$$

The natural expectation for this amplitude for ghost or DBI inflation is $f_{\text{NL}}^{\text{equil.}} \sim 100$, below the current constraints but at a level that should be attainable in the future. The limit an experiment can set on f_{NL} just scales as the inverse of the maximum l the experiment can detect. As a result, in the case of WMAP, increased observing time will approximately decrease the error bars by 30% and 60% for 4 years and 8 years of observation. The increased angular resolution and smaller noise of Planck pushes the point where noise dominates over signal to $l \sim 1500$. This should result in a factor of 4 improvement on the present constraints. In addition polarization measurements by Planck can further reduce the range by an additional factor of 1.6 [29].

We also constrained the presence of a 3-point function of the ‘‘local’’ type, predicted for example by the curvaton and variable decay width inflation models, obtaining

$$-27 < f_{\text{NL}}^{\text{local}} < 121 \quad \text{at 95\% C.L.} \quad (42)$$

We defined a quantity NG, which quantifies for any shape the level of non-Gaussianity of the data, analogously to the skewness for a single random variable. The limits on NG are very similar for the two shapes, approximately $|\text{NG}| < 0.02$ at 95% C.L. .

We showed that unless one has a full sky map with uniform noise, the estimator must contain a piece that is linear on the data in order to extract all the relevant information from the data and saturate the Cramer-Rao bound for the 3-point function measurement uncertainty. This correction is particularly important for the local shape and accounts for the improvement of our limits over that from the WMAP team. Moreover this correction goes a long way towards reducing the divergence in the variance of the estimator as l_{\max} is increased.

Acknowledgments

We would like to thank Eiichiro Komatsu for his help during the project, Eva Silverstein for volunteering to look into foreground contamination if we had found a positive signal, and Daniel Babich and Angelica de Oliveira-Costa for help with analysis software. The numerical analysis necessary for the completion of this paper was performed on the Sauron cluster, at the Center for Astrophysics, Harvard University, making extensive use of the HEALPix package [30]. LS is supported in part by funds provided by the U.S. Department of Energy (D.O.E) under cooperative research agreement DF-FC02-94ER40818. MZ was supported by the Packard and Sloan foundations, NSF AST-0506556 and NASA NNG05GG84G. MT was supported by NASA grant NAG5-11099, NSF grant AST-0134999, the Packard Foundation and Research Corporation.

References

- [1] J. Maldacena, “Non-Gaussian features of primordial fluctuations in single field inflationary models,” *JHEP* **0305**, 013 (2003) [astro-ph/0210603].
- [2] V. Acquaviva, N. Bartolo, S. Matarrese and A. Riotto, “Second-order cosmological perturbations from inflation,” *Nucl. Phys. B* **667**, 119 (2003) [astro-ph/0209156].
- [3] P. Creminelli and M. Zaldarriaga, “CMB 3-point functions generated by non-linearities at recombination,” *Phys. Rev. D* **70**, 083532 (2004) [astro-ph/0405428].
- [4] D. Babich, P. Creminelli and M. Zaldarriaga, “The shape of non-Gaussianities,” *JCAP* **0408**, 009 (2004) [astro-ph/0405356].
- [5] D. H. Lyth, C. Ungarelli and D. Wands, “The primordial density perturbation in the curvaton scenario,” *Phys. Rev. D* **67**, 023503 (2003) [astro-ph/0208055].
- [6] M. Zaldarriaga, “Non-Gaussianities in models with a varying inflaton decay rate,” *Phys. Rev. D* **69**, 043508 (2004) [astro-ph/0306006].
- [7] P. Creminelli, “On non-Gaussianities in single-field inflation,” *JCAP* **0310**, 003 (2003) [astro-ph/0306122].
- [8] N. Arkani-Hamed, P. Creminelli, S. Mukohyama and M. Zaldarriaga, “Ghost inflation,” *JCAP* **0404**, 001 (2004) [hep-th/0312100].
- [9] M. Alishahiha, E. Silverstein and D. Tong, “DBI in the sky,” *Phys. Rev. D* **70**, 123505 (2004) [hep-th/0404084].
- [10] L. Senatore, “Tilted ghost inflation,” *Phys. Rev. D* **71**, 043512 (2005) [astro-ph/0406187].
- [11] E. Komatsu *et al.*, “First Year Wilkinson Microwave Anisotropy Probe (WMAP) Observations: Tests of Gaussianity,” *Astrophys. J. Suppl.* **148**, 119 (2003) [astro-ph/0302223].

- [12] A. F. Heavens, “Estimating non-Gaussianity in the microwave background,” astro-ph/9804222.
- [13] D. Babich, “Optimal Estimation of Non-Gaussianity,” astro-ph/0503375.
- [14] L. M. Wang and M. Kamionkowski, “The cosmic microwave background bispectrum and inflation,” Phys. Rev. D **61**, 063504 (2000) [astro-ph/9907431].
- [15] E. Komatsu, D. N. Spergel and B. D. Wandelt, “Measuring primordial non-Gaussianity in the cosmic microwave background,” astro-ph/0305189.
- [16] Heron of Alexandria, *Metrica*, Alexandria, circa 100 B.C. – 100 A.D.
- [17] U. Seljak and M. Zaldarriaga, “A Line of Sight Approach to Cosmic Microwave Background Anisotropies,” Astrophys. J. **469**, 437 (1996) [astro-ph/9603033].
- [18] C. Bennett *et al.*, “First Year Wilkinson Microwave Anisotropy Probe (WMAP) Observations: Foreground Emission,” Astrophys. J. Suppl. **148**, 97 (2003) [astro-ph/0302208].
- [19] R. Juszkiewicz, D. H. Weinberg, P. Amsterdamski, M. Chodorowski and F. Bouchet, “Weakly nonlinear Gaussian fluctuations and the Edgeworth expansion,” Astrophys. J. **442** (1995) 39.
- [20] A. Taylor and P. Watts, “Parameter information from nonlinear cosmological fields,” Mon. Not. Roy. Astron. Soc. **328**, 1027 (2001) [astro-ph/0010014].
- [21] F. Bernardeau and L. Kofman, “Properties of the Cosmological Density Distribution Function,” Astrophys. J. **443** (1995) 479 [astro-ph/9403028].
- [22] G. Hinshaw *et al.*, “First Year Wilkinson Microwave Anisotropy Probe (WMAP) Observations: Angular Power Spectrum,” Astrophys. J. Suppl. **148**, 135 (2003) [astro-ph/0302217].
- [23] E. Komatsu, “The Pursuit of Non-Gaussian Fluctuations in the Cosmic Microwave Background,” astro-ph/0206039.
- [24] D. N. Spergel *et al.* [WMAP Collaboration], “First Year Wilkinson Microwave Anisotropy Probe (WMAP) Observations: Determination of Cosmological Parameters,” Astrophys. J. Suppl. **148**, 175 (2003) [astro-ph/0302209].
- [25] L. Page *et al.*, “First Year Wilkinson Microwave Anisotropy Probe (WMAP) Observations: Beam Profiles and Window Functions,” Astrophys. J. Suppl. **148**, 39 (2003) [astro-ph/0302214].
- [26] C. L. Bennett *et al.*, “First Year Wilkinson Microwave Anisotropy Probe (WMAP) Observations: Preliminary Maps and Basic Results,” Astrophys. J. Suppl. **148**, 1 (2003) [astro-ph/0302207].
- [27] M. Tegmark, A. de Oliveira-Costa & A.J.S. Hamilton, “A high resolution foreground cleaned CMB map from WMAP,” Phys. Rev. D **68**, 123523 (2003) [astro-ph/0302496].
- [28] L. Verde *et al.*, “First Year Wilkinson Microwave Anisotropy Probe (WMAP) Observations: Parameter Estimation Methodology,” Astrophys. J. Suppl. **148**, 195 (2003) [arXiv:astro-ph/0302218].
- [29] D. Babich and M. Zaldarriaga, “Primordial Bispectrum Information from CMB Polarization,” Phys. Rev. D **70**, 083005 (2004) [astro-ph/0408455].
- [30] K. M. Gorski, E. Hivon and B. D. Wandelt, “Analysis Issues for Large CMB Data Sets,” astro-ph/9812350.